



Real-time sub-Ångstrom imaging of reversible and irreversible conformations in rhodium catalysts and graphene

Christian Kisielowski,^{1,*} Lin-Wang Wang,² Petra Specht,³ Hector A. Calderon,⁴ Bastian Barton,⁵ Bin Jiang,⁶ Joo H. Kang,⁷ and Robert Cieslinski⁷

¹National Center for Electron Microscopy and Joint Center for Artificial Photosynthesis, Lawrence Berkeley National Laboratory, One Cyclotron Rd., Berkeley, California 94720, USA

²Material Sciences Division, Lawrence Berkeley National Laboratory, One Cyclotron Rd., Berkeley, California 94720, USA

³Department of Material Science & Engineering, University of California–Berkeley, Berkeley, California 94720, USA

⁴Dept. Fisica, ESFM-IPN, Mexico D.F. 07300, Mexico

⁵FEI Company, Eindhoven, The Netherlands

⁶FEI Company, 5350 NE Dawson Creek Drive, Hillsboro, Oregon 97124, USA

⁷The DOW Chemical Company, Midland, Michigan 48667, USA

(Received 8 May 2013; published 29 July 2013)

The dynamic responses of a rhodium catalyst and a graphene sheet are investigated upon random excitation with 80 kV electrons. An extraordinary electron microscope stability and resolution allow studying temporary atom displacements from their equilibrium lattice sites into metastable sites across projected distances as short as 60 pm. In the rhodium catalyst, directed and reversible atom displacements emerge from excitations into metastable interstitial sites and surface states that can be explained by single atom trajectories. Calculated energy barriers of 0.13 eV and 1.05 eV allow capturing single atom trapping events at video rates that are stabilized by the Rh [110] surface corrugation. Molecular dynamics simulations reveal that randomly delivered electrons can also reversibly enhance the sp^3 and the sp^1 characters of the sp^2 -bonded carbon atoms in graphene. The underlying collective atom motion can dynamically stabilize characteristic atom displacements that are unpredictable by single atom trajectories. We detect three specific displacements and use two of them to propose a path for the irreversible phase transformation of a graphene nanoribbon into carbene. Collectively stabilized atom displacements greatly exceed the thermal vibration amplitudes described by Debye-Waller factors and their measured dose rate dependence is attributed to tunable phonon contributions to the internal energy of the systems. Our experiments suggest operating electron microscopes with beam currents as small as zepto-amperes/nm² in a weak-excitation approach to improve on sample integrity and allow for time-resolved studies of conformational object changes that probe for functional behavior of catalytic surfaces or molecules.

DOI: [10.1103/PhysRevB.88.024305](https://doi.org/10.1103/PhysRevB.88.024305)

PACS number(s): 68.37.Lp, 61.80.Fe, 82.45.Jn

I. INTRODUCTION

In the recent past, significant initiatives have been dedicated to the exploration of sustainable energy solutions.^{1–6} Certainly, related research must address a rich diversity of challenges because it is not only the static arrangement of matter that must be understood at a single atom level but also its collective behavior that leads to functionality. Moreover, hybrid materials are now commonly explored to enable more complex functions. Traditionally, transmission electron microscopy (TEM) is considered the method of choice to unravel the static structure of materials at atomic resolution. This view is further strengthened by recent technological advancements, which enable atomic resolution at elevated temperature and pressure,^{7–10} dynamic electron microscopy with a time resolution of picoseconds or even femtoseconds^{11,12} at 0.3–0.4 nm of spatial resolution,¹² and aberration-corrected electron microscopy with deep, sub-Ångstrom resolution and single atom sensitivity.^{13–16} Such exceptional progress has nourished a growing expectation to provide equipment and concepts, which will enable capturing the dynamic behavior of matter with single atom sensitivity at atomic resolution in thermodynamically relevant conditions.

However, significant uncertainties must be addressed before the emerging visions can be forged into feasible experiments. In this respect, it is urgent to address the view that electrons of

mid-voltage energies around 300 keV and lower necessarily damage hybrid materials too much to maintain structural integrity at atomic resolution. In this energy range, there is a rapid displacement of atoms that are bonded to corners, edges, and surfaces of nanocrystals or catalysts since the binding energies to these sites are lowered compared with bulk values.^{17,18} In addition, ionization damage is known to be most hazardous to the soft matter components^{19–21} of hybrid materials. Of note, it is unsettled to date to what extent electron beam-induced structure alterations are reversible or irreversible.²² In the presence of strong beam-sample interactions, the achievable resolution is commonly described by:²³

$$d = (d_i^2 + (S/N)^2 / (C^{2*} D))^{1/2}. \quad (1)$$

Equation (1) relates the achievable resolution d to the image contrast C , the signal-to-noise ratio S/N , the accumulated electron dose D , and the native point resolution of the instrument d_i . In biological specimens, D cannot exceed ~ 1000 electrons/nm², which only allows resolving a few Ångstrom and prohibits single atom sensitivity.¹⁹ By comparison, the atomic resolution imaging of a single carbon atom in graphene sheets with a fair S/N ratio typically requires a sample exposure to 10^6 electrons/nm², which greatly exceeds threshold values for molecules. Therefore, atomic resolution

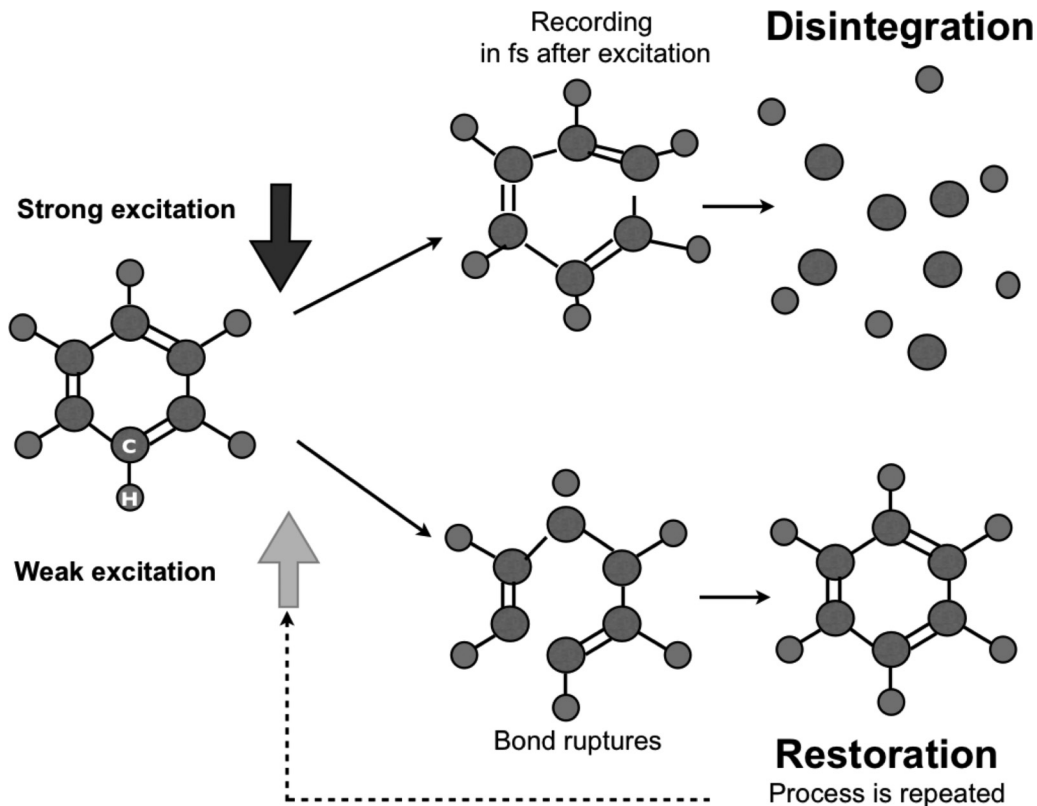


FIG. 1. Schematic representation of a strong excitation (top) and a weak excitation (bottom) experiment. For simplicity, a benzene ring is depicted, but the schematics may also describe any atom cluster on an undefined substrate.

imaging of molecules, small atom clusters or surface structures remains a grand challenge in basic sciences.²⁴

Consequently, new concepts are developed and tested that address atomic resolution imaging of radiation sensitive materials. A most successful approach pursues strong object excitations with x rays from a pulsed, free-electron laser.²⁵ The method builds on capturing diffraction patterns within femtoseconds after excitation to outrun the unavoidable material decomposition (Fig. 1, top). Alternatively, it is proposed to determine the three-dimensional (3D) conformations of macromolecular assemblies at atomic resolution from large data sets of images each recorded with an ultralow signal, $S/N \ll 3$ (Fig. 1, bottom),^{26,27} even beyond current practices in biological sciences. Implicitly, any such weak excitation method assumes that object excitations into higher energy states are reversible and not accompanied by uncontrolled atom loss, as symbolized at the top of Fig. 1. If such models apply, one would expect that dose rates dD/dt should become more important than the accumulated electron dose D in Eq. (1), and one could expect maintaining structural integrity at a larger accumulated electron dose if it is delivered at a small dose rate. Recent experiments with rhodium catalysts point to this direction.²⁸

This paper reports on previously uncontrolled phonon excitations that often dominate beam-sample interactions if atomic resolution imaging is practiced. It will be shown that such excitations can be tuned by electron dose rates to intentionally stimulate reversible or irreversible structure alterations. The finding opens room for the deployment of a weak-excitation approach for electron microscopy that also

allows exploring the gray zone between both extremes of Fig. 1. It is enabled by a recently developed in-line holography concept with dose rate variations by orders of magnitude at acceleration voltages between 20 kV and 300 kV.²⁹ The currently obtainable time resolution is in the range of minutes to milliseconds, and one can address turnover frequencies of chemical reactions for example. We demonstrate the validity of the concept by detecting phonon-assisted single atom trajectories and atom displacements by phonon excitations that create structure alterations relevant to the onset of functional system behavior.

II. RESULTS

A. Experimental details

Our experiments are performed with the Transmission Electron Aberration-Corrected TEAM 0.5 microscope operated at 80 kV. Details of its capabilities are published elsewhere.^{13,29} In brief, we achieve deep sub-Ångstrom resolution and long-time stability³⁰ by protecting an aberration-corrected status of the microscope with the voltage-dependent²⁹ and small chromatic-aberration coefficient C_c of an Ultra Twin objective lens³¹ and by narrowing the energy spread of the high-brightness Schottky field emitter with a monochromator.³² Residual lens aberrations are removed post-image acquisition during numerical reconstruction of the electron exit wave functions that creates the in-line holograms.³³ In this process, the recorded focus series of images are aligned to a precision of 2.4 pm.³⁴ The instrument is tuned to a negative spherical aberration coefficient $C_s = -15 \mu\text{m}$, and structural images

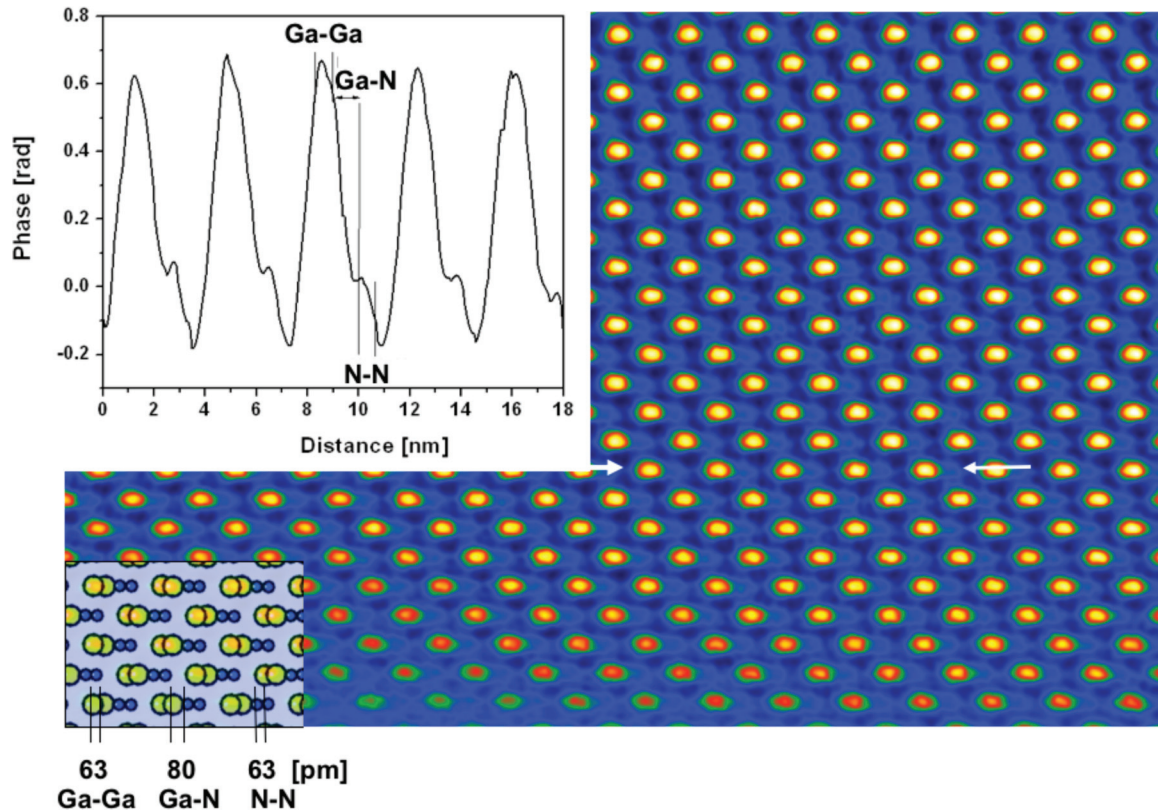


FIG. 2. (Color online) Phase image of a GaN [112] in-line hologram recorded at 80 kV. The contrast of the Ga and N columns differs largely because it scales with the atomic number $Z^{2/3}$. At the bottom of the image, the crystal is 1–2 nm thick. A structure model and a line profile are inserted showing the 80-pm separation of Ga and N dumbbells and the 63-pm separation within each Ga or N dumbbell. The elliptical shape of the Ga contrast in the lower half of the image is caused by the barely resolved Ga columns with a geometrical separation of 63 nm, as shown in the extracted line profile.

of thin samples occur at an overfocus of ~ 10 nm.³⁵ In this configuration, TEAM 0.5 exhibits an extraordinary small focus drift Δf_d of only 0.4 nm during minutes of recording time,²⁹ which is significantly smaller than the resolution limiting focus spread Δf_r of 0.7 nm.³³ The deep sub-Ångstrom resolution between 0.06 nm and 0.07 nm of the microscope at 80 kV is shown in Fig. 2 by resolving an adequate dumbbell spacing in GaN [112].

Since $\Delta f_d < \Delta f_r$, the acquired images are limited by resolution and not by drifting aberration coefficients.³⁰ This condition must be fulfilled to reliably interpret contrast changes across distances as small as 0.06 nm to 0.1 nm in experiments that last minutes. Further, we bypass the traditional condenser system using a new monochromator-assisted illumination scheme²⁸ and only expose sample areas of 400–900 nm² that are matched to the size of the charge-coupled device (CCD) camera at high resolution. Thereby, we eliminate any unnecessary sample exposure to the electron beam, which causes uncontrolled damage. In the past, attempts to approximate this situation were mostly sacrificed to accommodate a larger field of view. Moreover, the new illumination scheme allows for rapid dose rate adjustments by orders of magnitude.²⁸ Exposure times vary between 0.1 and 1 second, and the images are recorded with a sampling rate of 0.02–0.03 nm/pixel. For a detailed image analysis, the images are resampled on a 6-pm pixel grid using a bilinear extrapolation scheme, which is possible without increasing

noise because of the high S/N of better than 10:1 from one carbon atom in a reconstructed wave function. Our resampling process did not reach beyond 1/8 of a pixel size because smaller values approach the precision as to which images are aligned in the reconstruction process of the exit wave function. Other image processing routines include the extraction of an averaged motive and its standard deviation by cross-correlation averaging, which is a procedure that is commonly employed to boost the S/N s from identical objects in biological samples³⁶ and a solution to the phase problem by reconstruction of the complex electron-exit wave function from focus series of real space images.²⁹ The MacTempas software package³⁷ is used to apply these procedures. In addition, the software allows for image simulation by multislice calculations using theoretically predicted atom positions as input parameters.

Density functional theory (DFT) under the generalized gradient approximation (GGA)³⁸ is applied to calculate the graphene and rhodium systems. Projector-augmented wave pseudopotentials³⁹ are used as implemented in the Vienna *Ab initio* Simulation Package (VASP) code.⁴⁰ Transition path potential barriers are calculated by the nudged elastic band (NEB) method⁴¹ for a rhodium thin film slab that contains 144 atoms arranged in two monolayers. The behavior of interstitial atoms is calculated for the face-centered cubic (fcc) structure of rhodium using a periodic supercell containing 108 rhodium atoms arranged in $3 \times 3 \times 3$ fcc cubes with a $3 \times 3 \times 3$ Monkhorst-Pack k-point set for the supercell.

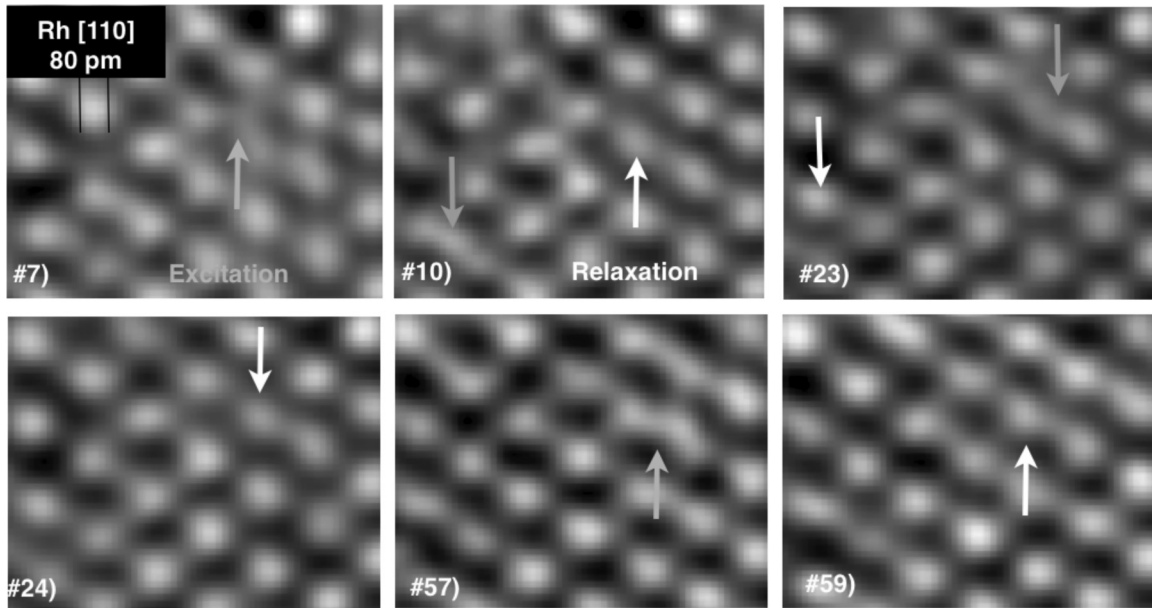


FIG. 3. Six structural images from a time series of 60 images of a rhodium catalyst in the [110] projection. Image acquisition numbers are listed. Dose rate is six 10^5 electrons/nm²/s. Gray arrows point to beam-induced atom displacements >60 pm that relax in successive frames (white arrows). The image contrast greatly fluctuates (see Supplemental Material, Ref. 48).

The periodic supercell for graphene contains 24 atoms and is used with $5 \times 5 \times 1$ Monkhorst-Pack k-points. *Ab initio* molecular dynamics (MD) simulations are carried out at average temperatures of 2500 K, 5000 K, 7500 K, and 10 000 K with time intervals of 2 fs. C-C bonds are constantly breaking and reforming at 10 000 K, and the graphene structure is lost. Therefore, we used 10 000 K as an approximate melting point temperature T_m of graphene. Experimentally, the solid/liquid phase transition temperature of graphite is ~ 4000 K (see Ref. 42), but it is known that the melting point of a graphene sheet is significantly higher because of absent interlayer carbon bonds.

Rhodium catalysts were prepared by impregnation of alumina with an aqueous solution of rhodium chloride and ammonium metatungstate to yield 2 wt% rhodium and a rhodium-to-tungsten ratio of 1. The impregnated catalyst was reduced in hydrogen at 300 °C and dispersed on holey carbon grids for observation. In the context of this paper, the catalysts are treated as rhodium crystals, and expectable contributions from the tungsten co-deposition will be reported elsewhere. The fabrication of exfoliated graphene sheets for imaging with electron beams has been reported and includes a prolonged exposure of single graphene layers to the high-energy electron beam. This removes all unwanted surface contaminants on a time scale of half an hour and eventually creates holes in exposed sample areas.⁴³ Finally, the strontium titanate (STO) samples are prepared in cross-section geometry by mechanical polishing, ion-beam processing, and thermal treatment. All measurements were done at room temperature.

B. Reversible atom displacements in a rhodium catalyst

Our investigation builds on previous reports about electron beam-induced atom displacements in thin films^{22,44,45} that are sample thickness dependent⁴⁶ and most prominent in surface

proximity and in nanocrystals consisting of a few atomic layers. A sequence of images from the central part of a rhodium catalyst is shown in Fig. 3 at a magnification that allows observing sub-Ångstrom atom displacements by visual inspection. Atom columns appear bright on a dark background and contain 2–3 atoms on average (thickness: ~ 0.6 nm).²² Since the phase contrast from atoms in thin films increases with their atomic number $Z^{2/3}$ ($Z_C = 6$, $Z_{Rh} = 45$, $Z_W = 74$; see Ref. 47), the rhodium contrast is strong and should be constant. Instead, it greatly fluctuates during observation, as reported earlier.²² There, the contrast fluctuations have been attributed to electron beam-induced phonon excitations resulting in 3D low frequency atom displacements, which are assumed to be random. A better impression of the seemingly continuous contrast fluctuations in the image series is provided in Movie-Rh (see Supplemental Material).⁴⁸ Expanding our previous work, Fig. 3 shows that such temporarily generated contrast appears systematically close to the projected tetragonal interstitial sites that are marked by I_T in Fig. 4(a). These sites are separated by a projected distance of only 95 pm from lattice site positions. Their 3D separation distance is 0.165 nm. Moreover, any contrast that is generated in the space between lattice sites also disappears in a successive frame of Fig. 3. Rarely, we detect similar contrast variations occurring close to the octahedral interstitial sites I_O [Fig. 4(a)], which suggests that they are not random but site specific. Equally important, the experiment documents that the crystal structure and its occupation with Rh atoms is maintained throughout the observation time. This requires that all underlying excitations are entirely reversible in suitably chosen current and voltage conditions. Thus, the randomly delivered electrons do not cause random excitations only. Instead, they thermalize into distinct metastable structures that can be observed and modeled as time-dependent deviations from an average structure, as shown next.

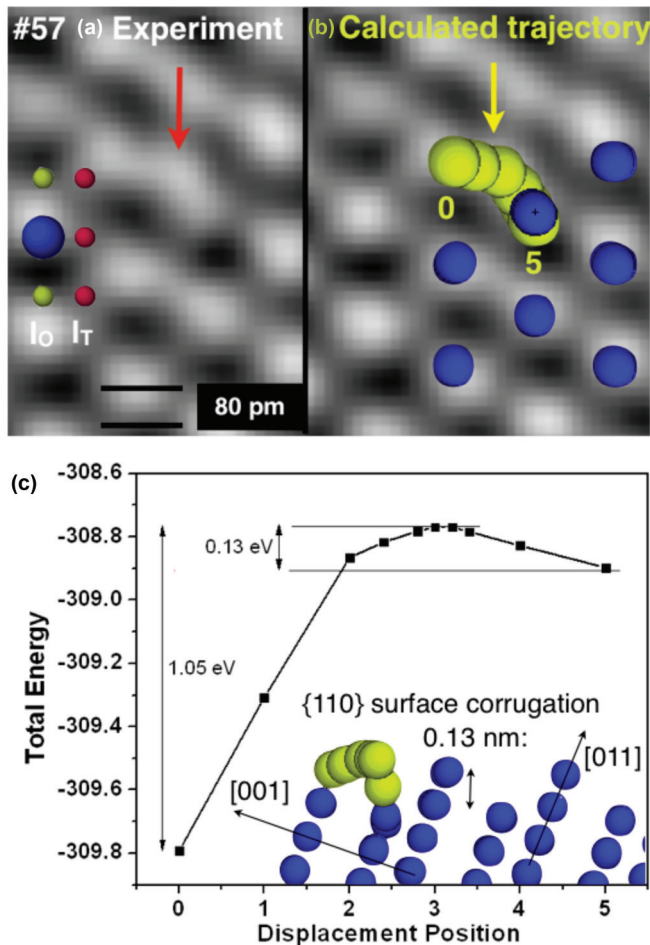


FIG. 4. (Color online) (a) Temporary atom displacement in frame 57 marked by arrow. Selected sites are pointed out. Dark circles are Rh lattice sites. Small light and dark circles are octahedral and tetrahedral interstitial sites I_O and I_T . (b) A calculated excitation/relaxation trajectory (0–5, bright circles) that matches the spatial distribution of the temporary image contrast in frame 57. (c) Total energy calculations for the displacement. Inset: Projected view of the corrugated Rh [110] surface in slab geometry.

First, we consider rhodium atoms that are displaced from their lattice site into interstitial sites and create Frenkel pairs. Such displacements are unstable if they occur in a nearest tetrahedral interstitial site because the generated interstitial/vacancy pair will recombine, as indicated from our DFT calculation. In contrast, an atom displacement into a second nearest tetrahedral site or the nearest octahedral site creates a metastable situation of prolonged lifetime. In the experiment, we rarely observe contrast formation in octahedral interstitial sites, and one must speculate about reasons why displacements into the second nearest tetrahedral interstitial sites are preferred. However, an agreement between the calculation and the experiment is achieved by considering atom trapping into surface states of the 0.6-nm-thin crystal. Results of these calculations are shown in Fig. 4(b) where the characteristic displacement trajectory of an excited Rh atom is described by steps 0 through 5 and is inserted into the experimental image. The excellent match of its path to the generated extra contrast between atom columns allows us to

identify this event as one origin for the temporary contrast generation. Figure 4(c) depicts total energy GGA calculations for this displacement, including the activation of a rhodium atom across an energy barrier of 1.05 eV for the excitation process and of 0.13 eV for recombination. Since total energy calculations typically underestimate barrier heights, we expect the actual barrier might be larger. These energies can be compared with binding energies between 1.7 eV and 4.6 eV for rhodium atoms in small clusters that decrease with decreasing crystal size.⁴⁹ Obviously, the internal energy of atoms bound in small clusters or to surfaces can be raised by electron irradiation to reach stability limits. Finally, the inserted view of the Rh crystal in Fig. 4(c) shows that the excited atom is temporarily captured in the channel of the corrugated [110] surface.

C. Reversible atom displacements in graphene

Having established a reasonable explanation for the contrast fluctuations, a deeper understanding of basic principles benefits from a simpler sample structure, which is why we resorted to investigating graphene, a single layer of sp^2 -bonded carbon atoms. The signature of temporary carbon atom displacements is even weaker in graphene than in rhodium because of the reduced scattering power of the light element. In essence, we aim now at the detection of a fractional contrast from a single carbon atom that may be as weak as the phase contrast signature from a single hydrogen atom. Therefore, we reduce noise by recording the focal series of 20 images from graphene that are reconstructed to obtain the complex electron exit wave function with an enhanced S/N .^{29,31}

A resulting phase image of graphene is shown in Fig. 5(a). It depicts its time-averaged structure at atomic resolution with a S/N that cannot be matched by another method using an equal electron dose at the given magnification. Again, we display the image at a large magnification to allow for an identification of irregularities by visual inspection. The two most recognizable events, A and B, are pointed out by arrows; a horizontal line eases the recognition of vertical atom displacements that reach tenths of picometers. The magnitude of the existing atom displacements from their equilibrium positions is determined by repetitively measuring the projected 0.14-nm C-C dumbbell distances across the entire image of Fig. 5(a) using a refined peak-fitting procedure. This method has been previously established and applied to extract the equivalent 0.14-nm Ga-As dumbbell distance in a 7-nm-thick GaAs sample.³⁴ Both measurements are compared in Fig. 5(b), and it is seen that the data spread $2\sigma = 46$ pm in graphene exceeds the equivalent GaAs value by a factor of 10. Next, we amplify contrast from additional but weaker site-specific displacements events in Fig. 5(a) by cross-correlating the hexagonal atom structure of graphene to every equivalent cell in the image, which allows calculating an average motive with an improved S/N and its standard deviation. The results are shown in Figs. 5(c) and 5(d), respectively. Of specific interest is the standard deviation image since it does not exhibit random noise but a modulated intensity pattern with accumulated contrast in positions A, B, and C. They are distinguishably different from the nearby lattice sites because of the sub-Ångstrom resolution of the instrument. In graphene,

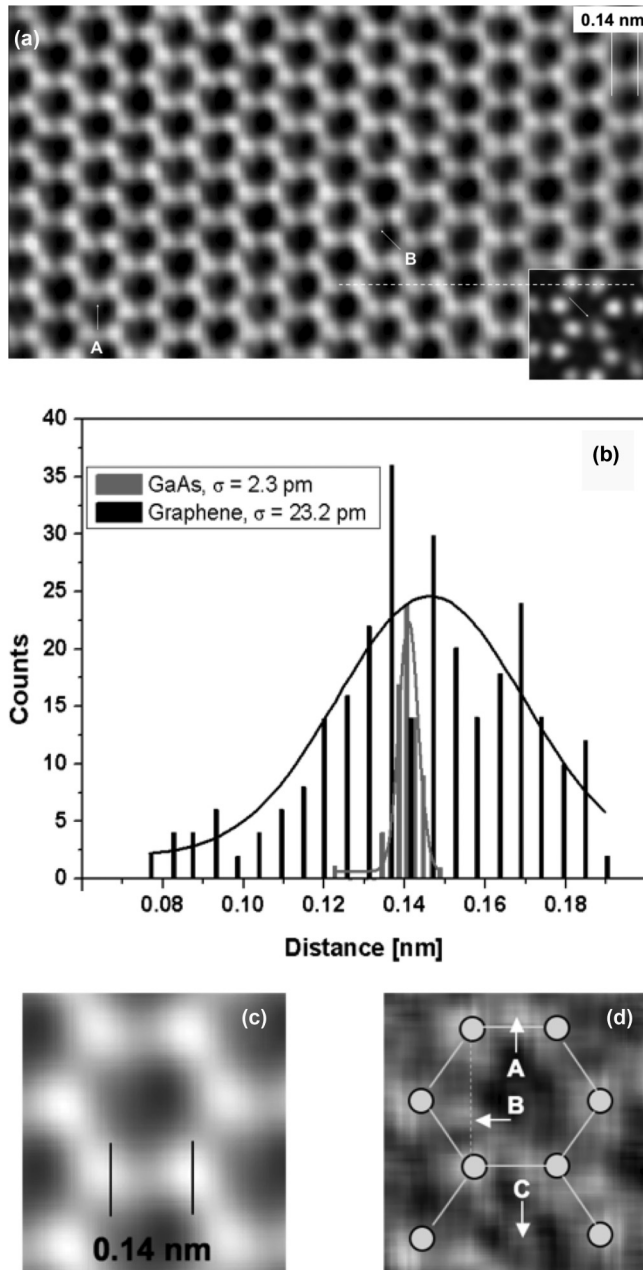


FIG. 5. (a) Phase image of graphene. Accumulated electron dose is four 10^7 electrons/nm². The inset is an image simulation of contrast fluctuations that are caused by atom displacements from MD simulations at $0.75T_m$. (b) Histogram of the C-C dumbbell distance in (a) and an equivalent measurement from GaAs.³⁴ (c) Average motive in (a). (d) The corresponding standard deviation amplifies reoccurring contrast in specific locations A, B, and perhaps C in unexpected sites.

however, both the large atom displacements from Fig. 5(b) and the accumulation of additional contrast in specific locations in Fig. 5(d) cannot be understood by modeling single atom trajectories since activation barriers for excitations are large and recombination is immediate.

We test the hypothesis that metastable states or eigenmodes can emerge from collective system excitations. Indeed, our MD simulations that are summarized in Figs. 6 and 7, and Table I strongly support this view. Figure 6(a) shows

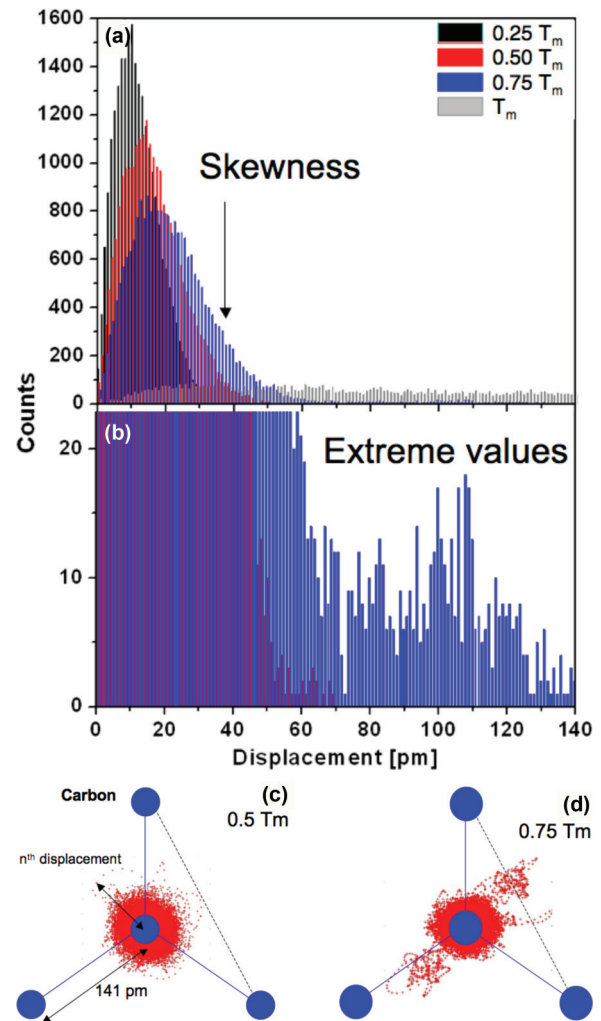


FIG. 6. (Color online) MD simulations at four different temperatures. (a) Histogram of the projected atom displacements from their equilibrium position highlighting the skewness of the distributions. (b) Magnified view emphasizing extreme displacement values >30 pm that exceed reasonable Debye-Waller factors for $0.5T_m$ and $0.75T_m$. Spatial distribution of 24 000 carbon atom displacements for (c) $0.5T_m$ and for (d) $0.75T_m$. The radius of the circles reflects the most common displacements (Debye-Waller factor).

histograms of calculated atom displacements that are extracted from 24 000 configurations of graphene and by a projection of the 3D atom displacements into an image plane. We consider four different temperatures between the melting point and a quarter of the melting point temperature. It is seen that the most common displacements u at the maximum of the distributions shift towards larger values with increasing temperature from 11 pm to 18 pm (Table I). If one attributes u to a Debye-Waller factor $B = 8\pi^2 u^2$, values between 1 and 3 Å² are calculated (Table I), which agree well with experimentally determined bulk values of graphites between 1–2 Å² at room temperature.⁵⁰ Most remarkable, however, is the pronounced skewness of the distribution that increases with temperature because of a rapidly increasing number of displacements larger than 30 pm, which certainly exceed reasonable values for Debye-Waller factors [Fig. 6(b)]. Table I lists the number of displacements larger than 30 pm as a

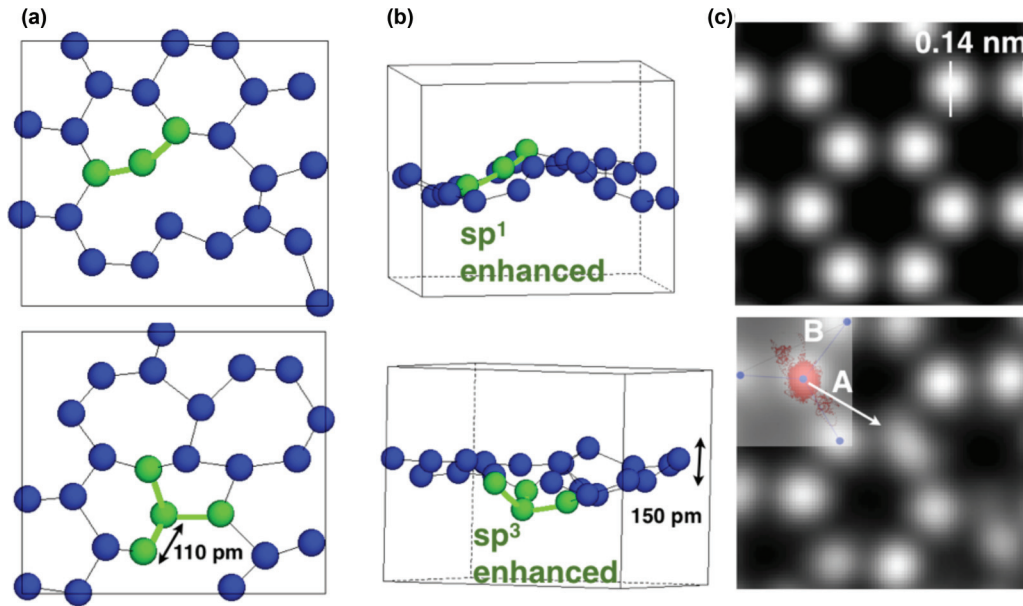


FIG. 7. (Color online) Two MD simulation snapshots at $0.75T_m$ of graphene in top view (a) and side view (b). (c) Lattice image by multislice simulations; top: static structure with $B = 1 \text{ \AA}^2$. Bottom: $B = 1 \text{ \AA}^2$ and using a 100-fs time average of the calculated MD configuration as an input. The inset is Fig. 6(d).

fraction of the total displacements. Such a ratio increases to 23% at $0.75T_m$. The spatial distribution of all atoms with respect to a central carbon atom and its next neighbors is shown in Figs. 6(c) and 6(d) for $0.5T_m$ and $0.75T_m$, respectively. A comparison of both figures highlights a dominantly random data distribution at low temperature. However, site-specific excitations emerge from this distribution into positions A and B as the temperature increases. At a temperature of $\sim 0.75T_m$, about a quarter of all displacements exceed 30 pm, which makes large atom displacement a most common event and detectable in micrographs with deep sub-Ångstrom resolution. Therefore, we conclude that random phonon excitations of the entire object can temporarily stabilize site-specific atom displacements, which we observe in the micrographs. Since such displacements are site specific (systematic), they do not vanish upon averaging. More generally, the question of how structure emerges in objects upon random excitations has sparked debates about entropy since the early developments of thermodynamic concepts.⁵¹

Figure 7 provides a better understanding of the phenomenon and its relation to the experiment. Two snapshots of the MD simulations are shown in top and side views. They both present significant deformations that the simulated graphene sheet

experiences upon thermal excitation [Figs. 7(a) and 7(b)]. Out-of-plane displacements occur with amplitudes as large as 0.15 nm. Thus, the sp^2 -bond character of carbon atoms in graphene is locally altered to include sp^1 - and sp^3 -bonding components that create chainlike structures and tetrahedral configurations locally. Fleeing ring structures are formed from five and seven carbon atoms. The difference between random and directed displacements in images from graphene is shown in Fig. 7(c) by multislice simulations. We assume a Debye-Waller factor $B = 1 \text{ \AA}^2$ to describe random displacements and utilize the calculated atom coordinates from the MD simulations to describe all directed displacements that occurred over a time period of 100 fs. The differences in such images (and in the corresponding phase images of a simulated electron exit wave function) are significant since directed structural changes cause contrast fluctuations and displacements far beyond values that one may expect from Debye-Waller factors. In particular, preferential displacements can be identified that include the sites A and B in this example, which are measured in the experiment as shown by the inset in Fig. 5(a). Therefore, we conclude that collective atom excitations can temporarily stabilize large atom displacements that occur irregularly in time as a result of a suitable displacement of many atoms and long-range interactions. One may call them rare events. In fact, it was reported earlier⁵² that the integration of long-range interactions into calculated phonon dispersions in graphite explains modes that include a translation of carbon atoms from their lattice site towards locations B and C, as observed in our experimental image in Fig. 5(d). In more general terms, we observe the channeling of random phonon excitations into a few site-specific displacements that point toward possible structural evolutions. It is tempting to apply this knowledge and predict a transformation path for the phase transformation of graphene into carbene.

TABLE I. Characteristic values of the projected bond-length distributions in graphene that are shown in Fig. 6(a).

Melting point temperature T_m	Maximum [pm]/Debye-Waller [\AA^2]	Displacements > 30 pm	Skewness
$\sim T_m$	-	23 925/99.7%	0.08
$0.75T_m$	18/2.6	5620/23%	1.75
$0.5T_m$	14/1.5	990/4%	0.81
$0.25T_m$	11/0.96	147/0.6%	0.49

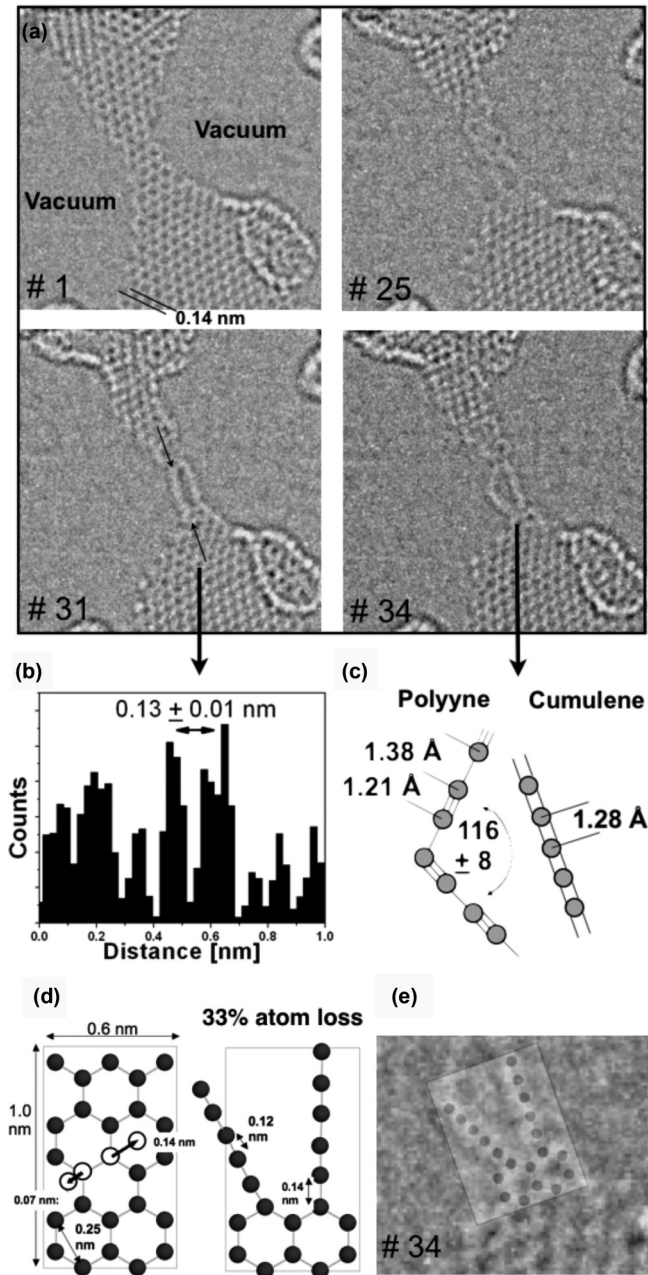


FIG. 8. (a) Time-resolved measurement of a carbene chain formation from a graphene bridge. Four frames of a time series of 40 images are shown. The time interval between successive images is 1.4 s. (b) Atomic resolution is obtained in frame 31. (c) Theoretical bond distances and models of polyynes and cumulenes are displayed. (d) Geometrical transformation of graphene into carbene as a result of atom displacements from lattice sites into positions B and C of Fig. 5(d). (e) Comparison of the model with the experiment in frame 34.

D. Irreversible phase transformation of graphene into carbene

A graphene sheet is transformed into linear chains of sp^1 -bonded carbon atoms by electron irradiation, as described in the literature.^{53,54} Movie-C in the Supplemental Material⁴⁸ depicts the entire process. Four snapshots of this phase transformation are displayed in Fig. 8(a). In frame 1, two adjacent holes are created by irradiation with a dose rate of five 10^6 electrons/ nm^2/sec , which remain separated by a

narrow graphene bridge. The bridge width is further reduced by preferentially removing carbon atoms from edge positions⁴³ until structure fluctuations occur in frame 25, and carbon chains form spontaneously that are ~ 1 nm long.

Surprisingly, the carbon chains remain stable during the extreme electron illumination and 13 successive images are acquired (frames 27–39; accumulated dose: nine 10^7 electrons/ nm^2) before the chains disintegrate in frame 40. Significant chain displacements occur during their observation, which are most obvious in Movie-C (see Supplemental Material),⁴⁸ but interchain cross-linking is not observed. In spite of their motion, atomic resolution is achieved in frame 31 and is shown in Fig. 8(b). In frame 34, a kink was formed with an angle of $(116 \pm 8)^\circ$ [Fig. 8(c)]. Topologically, the temporary formation of this kink from a previously straight line requires a chain length extension from 1.0 nm (includes nine carbon atoms) to 1.2 nm that must be accommodated by the addition of at least one extra carbon atom to the chain length if the average bond distance of 0.13 nm is to be preserved.

Short chains of carbon atoms are known as carbenes,⁵⁵ and they form polytypes with alternating single and triple bonds (polyynes) or double bonds (cumulenes) as shown in Fig. 8(c).⁵⁶ Kinks form on both polytypes with characteristic angles $\alpha = 115\text{--}120^\circ$ for polyynes and $\alpha' = 155\text{--}158^\circ$ for cumulenes.⁵⁶ Therefore, a measured kink angle of $(116 \pm 8)^\circ$ reveals that polyynes are formed in our experiments in agreement with the theoretical expectation that polyynes are more stable than cumulenes.⁵⁷ However, the beam-induced chain displacements also suggest that bond alterations among single, double, and triple bonds must occur just as in the case of graphene where hybridization is affected. Therefore, structure fluctuation between polyynes and cumulenes can occur, but they are undetectable by bond-length measurements within the experimental error of Fig. 8(b). Most remarkable is the fact that the chains do not disintegrate immediately in the high-energy electron beam but maintain conformations over extended time periods. Carbon atoms can even be added or removed from the chains. This unexpected behavior can be understood if one accepts that bonds break rapidly during the observation but reform faster than atoms can be removed. This process can be called “self-healing.”

Since possible phase transformation trajectories from graphene into carbene are unknown, we use now the measured excitations of carbon atoms in graphene in the locations B and C from Fig. 5(d) as a guideline to produce the geometrical transformation model shown in Fig. 8(d). The process is irreversible because it is accompanied by 33% atom loss. The detailed match of the resulting geometrical model with the experiment in Fig. 8(e) supports the interpretation that collective excitations direct the displacement of carbon atoms in the graphene bridge and stimulate this irreversible phase transition. Modeling single atom trajectories cannot capture this mechanism.

E. Dose rate dependences

Since the observed atom displacements are electron beam-induced, one must observe a contrast reduction in high-resolution images with an increasing dose rate (beam current). This contrast behavior becomes only observable after

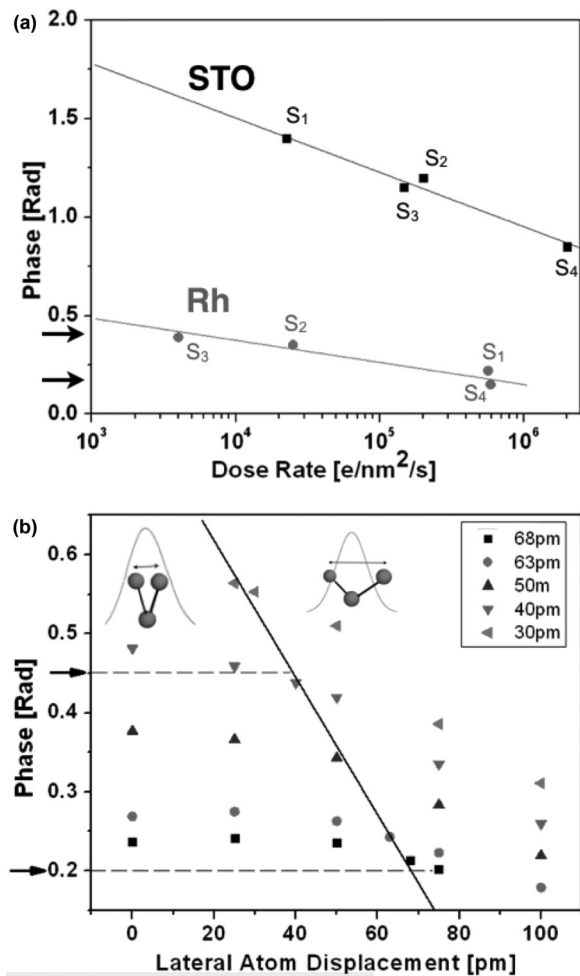


FIG. 9. (a) Measured logarithmic decrease of the image contrast with dose rates in phase images of reconstructed electron exit-wave functions. Focus series from identical areas of the rhodium catalysts and a STO confirmation sample were reconstructed from 60 images in a series. In S_i , $i = 1-4$, labels their recording sequence of a series. (b) Contrast in simulated-phase images from two rhodium atoms in an isolated column on lateral atom displacements of the top atom. Simulated phase images were reconstructed from simulated focus series of 10 images using the listed vibration amplitudes as an input to a Gaussian damping function. The solid line separates regions where the lateral displacements are either larger or smaller than the average vibration, as symbolized by the inserted schematics. Broken horizontal lines and arrows frame an identical phase range in (a) and (b).

minimizing experimental artifacts related to the CCD camera or to a sample drift. It must occur from a physical point of view because an increasing number of impinging electrons will rapidly increase local phonon emissions that successively displace atoms from their equilibrium position and soften the electron-scattering potential. For this reason, we acquire focal series of images with varying dose rates from the rhodium crystal and a STO confirmation sample. Figure 9(a) shows that contrast decreases logarithmically with the dose rate in both cases. In rhodium, it decreases by a factor of larger than two if the beam current increases from four 10³ electrons/nm²/s to six 10⁵ electrons/nm²/s. Contrast

losses by 50% or more are known as unexplainable mismatches between experimental images and image simulations.²⁸ Here, we find that they are caused by beam-induced phonon excitations. From the magnitude of the effect, one concludes that dynamic contributions to the image formation process can even exceed electron-scattering contributions from static objects in conditions for traditional high-resolution imaging. In view of this significant contrast loss, imaging in low dose rate conditions is greatly beneficial. In addition, there is significant room to study the dynamic behavior of matter by interpreting the dose rate dependence of contrasts, as demonstrated in this paper.

Alternatively, one may quote molecule motion across surfaces as a possible cause for a fluctuating contrast. However, the contrast change with the dose rate (0.5 rad measured compared with ~ 0.1 radian for the contrast of light atoms or molecules), and the reproducibility of the effect (data set Rh: S1 = S4 or data set STO: S2 = S3) that are shown in Fig. 9(a) exclude such interpretations.

In our image simulations, we distinguish between thermal excitations and dose rate effects using ordinary Debye-Waller factors of bulk materials and describe the beam-induced atom displacements by a Gaussian damping function with dose-rate-dependent vibration amplitudes. In the past, the procedure was used to accommodate mechanical microscope instabilities⁵⁸ that largely exceed the displacements, which we consider here. It is shown in Fig. 9(b) that damping amplitudes between 68 pm and 40 pm accurately describe the phase signal enhancement in Fig. 9(a), which is caused by decreasing dose rates from six 10⁵ electrons/nm²/s to four 10³ electrons/nm²/s. From the MD simulations of Fig. 6, one estimates that the difference of ~ 30 pm corresponds to a temperature reduction of $\sim 0.25T_m$ in the simulation. It is also seen that all lateral atom displacements smaller than the assumed damping amplitude are undetectable except for their contribution to a reduction of the average signal strength. Only if lateral displacements occur greater than the average damping amplitude and only if they exhibit a lifetime that is comparable to the image exposure time can they be captured in an image. In this sense, the finite image exposure time acts as a filter that enhances the detection of lateral structure alterations that present the successful attempts of the excited system to alter its structure.

III. DISCUSSION AND CONCLUSIONS

Egerton *et al.*²⁰ recently reviewed beam-sample interactions. Beyond their considerations, Jiang and Spence⁵⁹ suggested a spontaneous structure restoration as a possible mechanism for restoring material integrity upon sample excitation above threshold values. This aspect of self-healing is explored here by dose-rate-controlled aberration-corrected electron microscopy.

Figure 10(a) shows the available parameter space for such experiments in the TEAM 0.5 microscope by depicting the power $P = U \times I$, which is generated by a beam current I of electrons that are accelerated by a voltage U . Scaled to square meters, the available power can exceed 10¹² watts/m². Obviously, any small, absorbed fraction of this available power would vaporize any solid. However, the maximum power can easily be reduced by nine orders of magnitude upon current

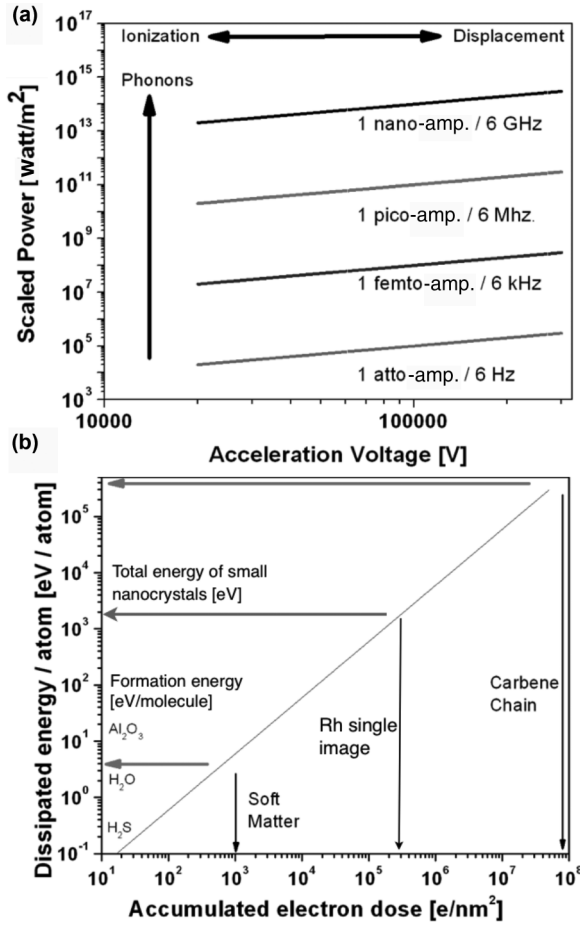


FIG. 10. (a) Available parameter space to perform dose-rate-dependent atomic resolution electron microscopy. Arrows point toward increasing beam-sample interactions as a result of specific interactions. (b) Energy deposition in carbon materials. Characteristic, accumulated electron doses are marked and compared with formation energies of selected molecules or nanocrystals.

reduction only. Atomic resolution imaging with atto-amperes or less, however, would hardly create contrast above noise with typical image exposure times of 1 second. Therefore, we employ in-line holography to create a single image from hundreds of frames that are recorded over several minutes.²⁹ Acceleration voltages can be altered between 20 kV and 300 kV while maintaining atomic resolution.²⁹ Compared with current variations, such voltage differences change the power deposition marginally. Nonetheless, beam-sample interactions are most commonly discussed in the context of voltage-dependent ionization or displacement damage,²⁰ which are certainly relevant processes that are rarely distinguished from beam-induced phonon excitations. The present phonon excitations are well documented in early work⁶⁰ and in recent time-resolved measurements.¹² Such time-resolved measurements also suggest that we do not observe short time excitations in the electronic structure of the materials but atomic motions in the thermalization process. In this regime, the lifetime of phonons approaches the average delivery time for electrons, which is set by dose rates. As a result, we expect observing dose-rate-dependent contrast modulations. The relevance of reversible excitations becomes obvious if one estimates the

energy E per volume V , which is dissipated in the sample and by⁶¹

$$E/V = n^* \rho^* dE/dx. \quad (2)$$

Here, n is the accumulated number of impinging electrons per unit area, ρ is the material density, and dE/dx is the stopping power, e.g., the energy dissipated per unit per mass thickness. This estimate is shown in Fig. 10(b), where we used $\rho = 3.5 \text{ g/cm}^3$, $dE/dx = 3 \times 10^6 \text{ eV/cm}^2/\text{g}$ (at 60 kV) and 177 carbon atoms/nm³ for the specific case of the cubic diamond structure. We consider the accumulated electron dose only, which obviously omits any rate dependences. For a light element such as carbon, two-thirds of all scattering events are inelastic. Moreover, the energy densities are compared with formation energies of selected molecules and with total energies of small nanocrystals that may contain 1000 atoms or so. It is seen that an accumulated dose of only 1000 electrons/nm² already increases the inner energy per carbon atom by several electron volts, which already exceeds the formation energy of water molecules during observation. Therefore, it seemed reasonable to accept such low dose values as an upper boundary for damage-free imaging of soft matter, as practiced for biological samples. In atomic resolution imaging, an accumulated dose of typically 10⁵–10⁶ electrons/nm² is used, which most certainly exceeds any reasonable binding energy of single atoms. Even if this energy is shared between ~1000 atoms, an excitation of a few electron volts per atom would remain, which is enough to cause sample decomposition or melting. In light of this estimate, it should be entirely impossible to image a single chain of 10 carbon atoms with an accumulated dose of 10⁸ electrons/nm² (Fig. 8) without acknowledging the existence of reversible excitations and a concept of self-healing.

It is interesting considering how the available energy is stored in the object. Unlike using a conventional illumination system in transmission electron microscopy, we match the illuminated sample area to the field of view defined by the CCD camera, which allows us to control the number of scattering events in the sample and tune the inner energy of the system. Using a beam current of 10⁵–10⁶ electrons/nm²/s and a 30 nm × 30 nm large field of view, 10⁸–10⁹ high-energy, inelastic scattering events occur in each second if every electron participates. Most obvious contributions to the internal energy U of an elastic medium include

$$U = T S + 1/2 \sigma_{ij} \epsilon_{ij}. \quad (3)$$

Here, T is temperature, S is entropy, and $\frac{1}{2} \sigma_{ij} \epsilon_{ij}$ is the elastic energy described by general expressions for stress and strain, respectively. It is beyond the scope of this paper to quantitatively untangle all contributions from beam-sample interactions to the internal energy of the investigated samples at this point. Instead, it is noted that time-resolved TEM experiments with graphite are currently performed that aim to perform this task with femtoseconds of time resolution and a spatial resolution of a few Ångstrom.¹² Concerning the structural dynamics of graphite⁶² or graphene, a converging view emerges that Debye-Waller factors alone cannot explain the measured mean-square atom displacements in excited samples. Instead, their explanation requires a strong coupling of phonons and many particle interactions.

In our simulations, the increase of internal energy is entirely attributed to temperature, which would increase by hundreds of degrees in high dose rate conditions unless temperature is rapidly channeled into the substrate that holds the investigated samples in place. Alternatively, entropy would moderate any temperature increase since it contributes to the specific heat of materials through the logarithm of a partition function. An expected logarithmic contribution of the numerous beam-induced object vibrations to the internal energy of samples is consistent with the observed logarithmic dependence of image contrast on dose rates. Both aspects are quite relevant since dynamic measurements of a phase transition in Cu₂S nanocrystals recently verified that a sample irradiation with a high dose rate increases temperature by only a few degrees,⁶³ and it is known that electron beam-induced temperature increases can be small.⁶⁴ Elastic contributions to the internal energy would increase quadratically with increasing atom displacements and appear most prominent in small nanocrystals, thin films, and in surface proximity, where binding energies are lowered and materials are more flexible. Again, this expectation is in agreement with our experimental results.^{17,22,45,46}

Finally, our investigations allow for unambiguous interpretations because we intentionally investigated simple structures. Investigations of more complex systems are being pursued now and will be published soon. In this paper, the detection of single atom trajectories by electron microscopy and the observed dynamic stabilization of characteristic displacements in graphene are reported, which could only be accomplished by applying deep sub-Ångstrom electron microscopy at 80 kV using a microscope of extraordinary stability. Further, we point out that collective sample excitations probe the potential energy surface of a sample more completely than state-of-the-art calculations using single atom trajectories⁶⁵ and that the detection of extreme displacement values is of general interest in modeling rare but significant events.⁶⁶ Beyond these findings, the paper establishes a weak excitation approach for electron microscopy that is compatible with environmental⁹ and time-resolved¹² TEM in broad-beam mode. Certainly, ionization or displacement of atoms proceeds constantly during the imaging process at any voltage and

current, and it will set an ultimate limit to the application of electron microscopy. Here we stress that contributions of phonon excitations are equally relevant and demonstrate that the existence of reversible system excitations matters greatly since it delays sample degradation to an unexplored end.

ACKNOWLEDGMENTS

C.K. acknowledges fruitful discussions with P. Schwander and A. Ourmazd about their weak excitation approach, which they call “divide and conquer,” and with S. Helveg about beam-sample interactions in electron microscopy and the relevance of these findings to chemical reaction pathways. Moreover, C.K. is grateful to N. Alem and Y. Li for the fabrication of electron-transparent samples of graphene and STO, respectively. Electron microscopy was performed at NCEM, which is supported by the Office of Science, Office of Basic Energy Sciences of the US Department of Energy under Contract No. DE-AC02-05CH11231. The Dow Chemical Company supported P. Specht for the investigations of the rhodium catalysts. B.B. and H.A.C. were supported by Helios SERC project to develop and apply low dose rate microscopy. H.A.C. also acknowledges support through CONACYT (Grant No. 129207-FOINS75/2012). The work on collective excitations in carbon materials was performed for the Joint Center for Artificial Photosynthesis, a DOE Energy Innovation Hub, supported through the Office of Science of the US Department of Energy under Award No. DE-SC0004993. Calculations were supported by the Office of Science, Office of Basic Energy Sciences, Materials Science and Engineering Division (MSE) of the US Department of Energy under Contract No. DE-AC02-05CH11231. The investigation uses resources of the National Energy Research Scientific Computer Center (NERSC) and resources of the Oak Ridge Leadership Computing Facility located at the National Center for Computational Science, which is supported by the Office of Science, Office of Basic Energy Sciences of the US Department of Energy under Contract No. DE-AC05-000R22775. Computer time was allocated by DOE’s Innovative and Novel Computational Impact on Theory and Experiment (INCITE) Program.

*Corresponding author: cfkisielowski@lbl.gov

¹W. U. Huynh, J. J. Dittmer, and A. P. Alivisatos, *Science* **295**, 2425 (2002).

²N. S. Lewis and D. G. Nocera, *Proc. Nat. Acad. Sci. USA* **103**, 15729 (2006).

³S. Y. Reece, J. A. Hamel, K. Sung, T. D. Jarvi, A. J. Esswein, J. J. H. Pijpers, and D. G. Nocera, *Science* **334**, 645 (2011).

⁴<http://carboncycle2.lbl.gov/> (2013).

⁵<http://solarfuelshub.org/> (2013).

⁶http://www.k-cap.or.kr/e_index.html (2013).

⁷S. Chenna and P. A. Crozier, *ACS Catalysis* **2**, 2395 (2012).

⁸J. F. Creemer, S. Helveg, G. H. Hovelings, S. Ullmann, A. M. Molenbroek, P. M. Sarro, and H. W. Zandbergen, *Ultramicroscopy* **108**, 993 (2008).

⁹H. Yoshida, Y. Kuwauchi, J. R. Jinschek, K. Sun, S. Tanaka, M. Kohyama, S. Shimada, M. Haruta, and S. Takeda, *Science* **335**, 317 (2012).

¹⁰J. R. Jinschek and S. Helveg, *Micron* **43**, 1156 (2012).

¹¹N. D. Browning, M. A. Bonds, G. H. Campbell, J. E. Evans, T. LaGrange, K. L. Jungjohann, D. J. Masiel, J. McKeown, S. Mehraeen, B. W. Reed, and M. Santala, *Current Opinion in Solid State Science* **16**, 23 (2012).

¹²A. H. Zewail, *Sci. Am.* **303**, 74 (2010).

¹³C. Kisielowski, B. Freitag, M. Bischoff, H. van Lin, S. Lazar, G. Knippels, P. Tiemeijer, M. van der Stam, S. von Harrach, M. Stekelenburg, M. Haider, S. Uhlemann, H. Mueller, P. Hartel, B. Kabius, D. Miller, I. Petrov, E. A. Olson, T. Donchev *et al.*, *Microsc. Microanal.* **14**, 454 (2008).

- ¹⁴R. Erni, M. D. Rossell, C. Kisielowski, and U. Dahmen, *Phys. Rev. Lett.* **102**, 096101 (2009).
- ¹⁵N. Alem, O.-V. Yazyev, C. Kisielowski, P. Denes, U. Dahmen, P. Hartel, M. Haider, S. Uhlemann, B. Jiang, S. G. Louie, and A. Zettl, *Phys. Rev. Lett.* **106**, 126102 (2011).
- ¹⁶O. L. Krivanek, M. F. Chisholm, V. Nicolosi, T. J. Pennycook, G. J. Corbin, N. Dellby, M. F. Murfitt, S. S. Own, Z. S. Szilagyi, M. P. Oxley, S. T. Pantelides, and S. J. Pennycook, *Nature* **464**, 571 (2010).
- ¹⁷A. V. Martin, K. Ishizuka, C. Kisielowski, and L. J. Allen, *Phys. Rev. B* **74**, 172102 (2006).
- ¹⁸R. M. Wang, O. Dmitrieva, M. Farle, G. Dumpich, H. Q. Ye, H. Poppa, R. Kilaas, and C. Kisielowski, *Phys. Rev. Lett.* **100**, 017205 (2008).
- ¹⁹R. M. Glaeser, K. Downing, D. De Rosier, W. Chiu, and J. Frank, *Electron Crystallography of Biological Macromolecules* (Oxford University Press, New York, 2009), pp. 131–134.
- ²⁰R. F. Egerton, P. Li, and M. Malac, *Micron* **35**, 399 (2004).
- ²¹B. E. Bammes, J. Jakana, M. F. Schmid, and W. Chiu, *J. Struct. Biol.* **169**, 331 (2010).
- ²²P. Specht, R. J. Gulotty, D. Barton, R. Cieslinski, S. Rozeveld, J. H. Kang, O. D. Dubon, and C. Kisielowski, *ChemCatChem* **3**, 1034 (2011).
- ²³A. Rose, *J. Opt. Soc. Am.* **38**, 196 (1948).
- ²⁴J. Hemminger, chair, Basic Energy Sciences Advisory Committee, Directing matter and energy: Five challenges for science and the imagination, <http://science.energy.gov/bes/news-and-resources/reports/basic-research-needs/> (2013).
- ²⁵H. N. Chapman, P. Fromme, A. Barty, T. A. White, R. A. Kirian, A. Aquila, M. S. Hunter, J. Schulz, D. P. DePonte, U. Weierstall, R. B. Doak, F. R. N. C. Maia, A. V. Martin, I. Schlichting, L. Lomb, N. Coppola, R. L. Shoeman, S. W. Epp, R. Hartmann *et al.*, *Nature* **470**, 72 (2011).
- ²⁶R. Fung, V. Shneerson, D. K. Saldin, and A. Ourmazd, *Nature Physics* **5**, 64 (2009).
- ²⁷P. Schwander, R. Fung, G. N. Phillips, and A. Ourmazd, *New J. Phys.* **12**, 035007 (2010).
- ²⁸A. Howie, *Ultramicroscopy* **98**, 73 (2004).
- ²⁹B. Barton, B. Jiang, C. Y. Song, P. Specht, H. Calderon, and C. Kisielowski, *Microsc. Microanal.* **18**, 982 (2012).
- ³⁰S. M. Schramm, S. J. van der Molen, and R. M. Tromp, *Phys. Rev. Lett.* **109**, 163901 (2012).
- ³¹C. Kisielowski, C. J. D. Hetherington, Y. C. Wang, R. Kilaas, M. A. O’Keefe, and A. Thust, *Ultramicroscopy* **89**, 243 (2001).
- ³²P. C. Tiemeijer, M. Bischoff, B. Freitag, and C. Kisielowski, *Ultramicroscopy* **114**, 72 (2012).
- ³³P. C. Tiemeijer, M. Bischoff, B. Freitag, and C. Kisielowski, *Ultramicroscopy* **118**, 35 (2012).
- ³⁴X. Xu, S. P. Beckman, P. Specht, E. R. Weber, D. C. Chrzan, R. P. Erni, I. Arslan, N. Browning, A. Bleloch, and C. Kisielowski, *Phys. Rev. Lett.* **95**, 145501 (2005).
- ³⁵M. Lentzen, *Microsc. Microanal.* **14**, 16 (2008).
- ³⁶O. W. Saxton and W. Baumeister, *J. Microsc.* **127**, 127 (1982).
- ³⁷<http://www.totalresolution.com>.
- ³⁸J. P. Perdew, K. Burke, and M. Ernzerhof, *Phys. Rev. Lett.* **77**, 3865 (1996).
- ³⁹G. Kresse and D. Joubert, *Phys. Rev. B* **59**, 1758 (1999).
- ⁴⁰<http://www.vasp.at>.
- ⁴¹G. Henkelman, B. P. Uberuaga, and H. Jonsson, *J. Chem. Phys.* **113**, 9901 (2000).
- ⁴²A. G. Whittaker, *Science* **200**, 763 (1978).
- ⁴³Ç. Ö. Girit, J. C. Meyer, R. Erni, M. D. Rossell, C. Kisielowski, L. Yang, C.-H. Park, M. F. Crommie, M. L. Cohen, S. G. Louie, and A. Zettl, *Science* **323**, 1705 (2009).
- ⁴⁴N. Alem, R. Erni, C. Kisielowski, M. D. Rossell, W. Gannett, and A. Zettl, *Phys. Rev. B* **80**, 155425 (2009).
- ⁴⁵C. Kisielowski, Q. M. Ramasse, L. P. Hansen, M. Brorson, A. Carlsson, A. M. Molenbroek, H. Topsøe, and S. Helveg, *Angew. Chem., Int. Ed.* **49**, 2708 (2010).
- ⁴⁶D. Alloyeau, B. Freitag, S. Dag, L.-W. Wang, and C. Kisielowski, *Phys. Rev. B* **80**, 014114 (2009).
- ⁴⁷E. J. Kirkland, *Advanced Computing in Electron Microscopy* (Springer-Verlag, New York, 2010).
- ⁴⁸See Supplemental Material at <http://link.aps.org/supplemental/10.1103/PhysRevB.88.024305> for Movie-Rh.avi and Movie-C.avi.
- ⁴⁹L. Wang and Q. Ge, *Chem. Phys. Lett.* **366**, 368 (2002).
- ⁵⁰T. Abe, Y. Mizutani, N. Shinoda, M. Asano, T. Harada, and M. Murakami, *J. Phys. Chem.* **57**, 783 (1996).
- ⁵¹V. S. Steckline, *Am. J. Phys.* **51**, 894 (1983).
- ⁵²L. Wirtz and A. Rubio, *Solid State Commun.* **131**, 141 (2004).
- ⁵³C. Jin, H. Lan, L. Peng, K. Suenaga, and S. Iijima, *Phys. Rev. Lett.* **102**, 205501 (2009).
- ⁵⁴A. Chuvilin, J. C. Meyer, G. Algara-Siller, and U. Kaiser, *New J. Phys.* **11**, 083019 (2009).
- ⁵⁵K. S. Pitzer and E. Clementi, *J. Am. Chem. Soc.* **81**, 4477 (1959).
- ⁵⁶R. B. Heinemann, J. Kleiman, and N. M. Salansky, *Nature* **306**, 164 (1983).
- ⁵⁷M. J. Rice, S. R. Phillpot, A. R. Bishop, and D. K. Campbell, *Phys. Rev. B* **34**, 4139 (1986).
- ⁵⁸M. A. O’Keefe, *Ultramicroscopy* **47**, 282 (1992).
- ⁵⁹N. Jiang and J. H. C. Spence, *Ultramicroscopy* **113**, 77 (2012).
- ⁶⁰B. Schroeder and J. Geiger, *Phys. Rev. Lett.* **28**, 301 (1972).
- ⁶¹L. Raimier, *Transmission Electron Microscopy* (Springer, Optical Series, New York, 1993).
- ⁶²S. Schaefer, W. Liang, and A. H. Zevail, *New J. Phys.* **13**, 063030 (2011).
- ⁶³H. Zheng, J. B. Rivest, T. A. Miller, B. Sadtler, A. Lindenberg, M. F. Toney, L.-W. Wang, C. Kisielowski, and A. P. Alivisatos, *Science* **333**, 206 (2011).
- ⁶⁴B. Jouffrey and M. Karlik, *Microscopy Microanalysis Microstructure* **3**, 243 (1992).
- ⁶⁵F. Abild-Pedersen, J. K. Nørskov, J. R. Rostrup-Nielsen, J. Sehested, and S. Helveg, *Phys. Rev. B* **73**, 115419 (2006).
- ⁶⁶P. Joyce, D. R. Rokyta, C. J. Beisel, and H. A. Or, *Genetics* **180**, 1627 (2008).